

Plug-and-Play Single-Photon Devices with Efficient Fiber-Quantum Dot Interface

Woong Bae Jeon, Jong Sung Moon, Kyu-Young Kim, Young-Ho Ko, Christopher J. K. Richardson, Edo Waks, and Je-Hyung Kim*

Incorporating solid-state quantum emitters into optical fiber networks enables the long-distance transmission of quantum information and the remote connection of distributed quantum nodes. However, interfacing quantum emitters with fiber optics encounters several challenges, including low coupling efficiency and delicate configuration. In this study, a highly efficient fiber-interfacing photonic device that directly launches single photons from quantum dots into a standard FC/PC-connectorized single-mode fiber is demonstrated. Optimally designed photonic structures based on hole gratings produce an ultra-narrow directional beam that matches the small numerical aperture of a single-mode fiber. A pick-and-place technique precisely integrates a single miniaturized device into the core of the fiber. This approach realizes a plug-and-play single-photon device that does not require optical alignment and thus guarantees long-term stability. The results represent a major step toward practical and reliable transmission of quantum light across a fiber network.

1. Introduction

Solid-state quantum dots (QDs) with a variety of exciton states provide important quantum building blocks such as single

photons,^[1–3] entangled photon pairs,^[4–6] and spin memories^[7] for quantum information processing. Recent advances in material growth, nanofabrication, and coherent control techniques for QDs have led to the realization of quantum communication,^[5,8–11] quantum teleportation,^[12,13] and quantum simulations.^[3] Moreover, QDs can mediate the quantum interaction between spins and photons^[14,15] or between photons and photons,^[16] thus creating deterministic quantum gates^[16,17] and photonic cluster states.^[18] The problem of spectral inhomogeneity in solid-state quantum emitters can be addressed via temporal-to-spatial demultiplexing^[19,20] and local frequency tuning^[21–23] techniques, enabling the production of multiple indistinguishable single photons and resonant emitters for scalable

quantum systems. To implement the above quantum technologies in a practical way, it is essential to interface quantum emitters with low-loss optical platforms. Well-developed fiber optics provide an ideal platform for establishing scalable and distributed quantum systems.^[5,24,25]

There have been several different approaches for coupling single-photon emissions from QDs into fiber optics. Most straightforwardly, a piece of a QD wafer can be directly attached to an optical fiber.^[26] This simple integration lacks coupling efficiency owing to QD emission with poor light extraction and non-Gaussian far-field patterns. Intermediate optical systems^[27,28] or microstructured optical fibers^[29] can improve fiber coupling efficiency; however, continuous adjustment of the optical alignment is unavoidable to maintain this efficiency. Integrating QDs into 3D micro/nanophotonic structures, such as micropillars,^[30,31] nanowires,^[32] and monolithic lenses^[33–35] can significantly enhance light extraction and produce Gaussian-like far-field patterns. However, these methods are based on chip-to-fiber integration, which wastes samples and limits scalability. Ideally, adiabatic coupling between a tapered single-photon device and a fiber can realize single device-to-fiber integration.^[36,37] Although such integration can produce near-unit coupling efficiency,^[38] the delicate tapered structures cause long-term stability problems. Therefore, the efficient and reliable implementation of fiber-integrated quantum emitters remains a challenging goal.

In this study, we demonstrate efficient and compact plug-and-play single-photon sources based on telecom wavelength emitting QDs with hole-based circular Bragg gratings (hole-CBGs).


W. B. Jeon, J. S. Moon, K.-Y. Kim, J.-H. Kim
Department of Physics
Ulsan National Institute of Science and Technology (UNIST)
Ulsan 44919, Republic of Korea
E-mail: jehyungkim@unist.ac.kr

Y.-H. Ko
Electronics and Telecommunications Research Institute
Daejeon 34129, Republic of Korea

C. J. K. Richardson
Laboratory for Physical Sciences
University of Maryland
College Park, MD 20740, USA

E. Waks
Department of Electrical and Computer Engineering and Institute for
Research in Electronics and Applied Physics
University of Maryland
College Park, MD 20742, USA

E. Waks
Joint Quantum Institute
University of Maryland and the National Institute of Standards and
Technology
College Park, MD 20742, USA

 The ORCID identification number(s) for the author(s) of this article can be found under <https://doi.org/10.1002/qute.202200022>

DOI: 10.1002/qute.202200022

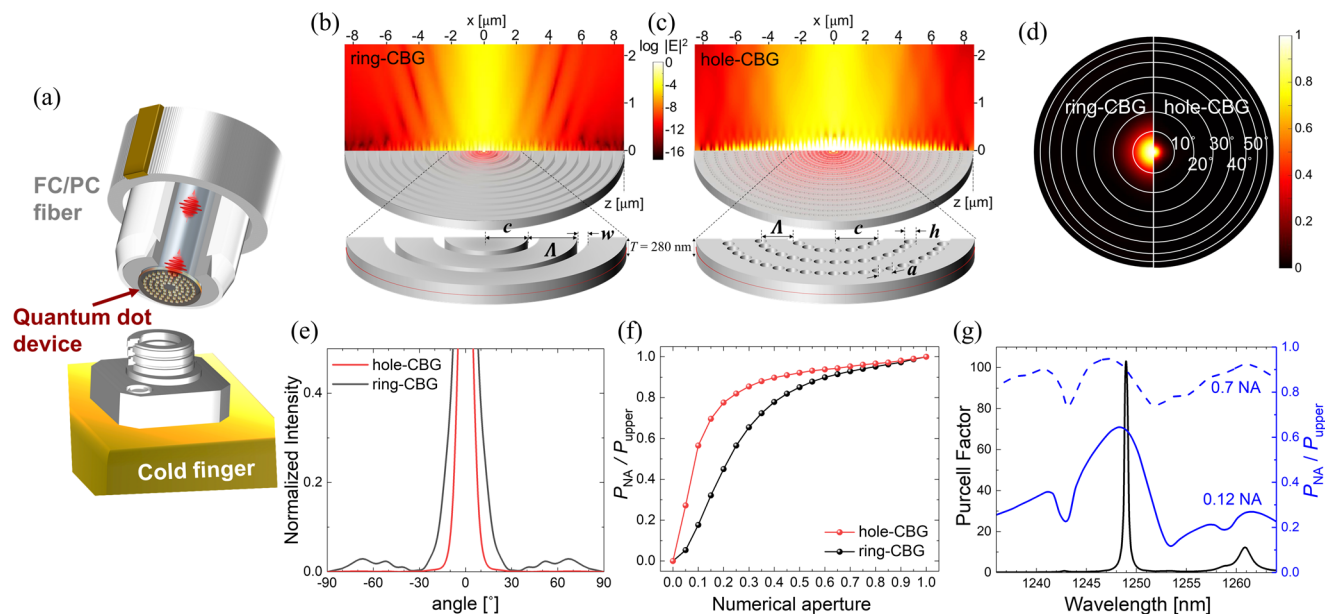


Figure 1. Ultra-narrow vertical beam in a hole-CBG. a) Schematic image of a hole-CBG device integrated into a single-mode fiber. The hole-CBG device includes InAs/InP QDs. The integrated fiber–QD device can be stably mounted on a cold finger using an FC/PC mating sleeve for low-temperature operation. Schematics and simulation results of b) a ring-CBG and c) a hole-CBG, respectively. The vertical cross-sectional field profiles show the normalized $|E|^2$ for each device on a logarithmic scale. The in-plane spatial field ($|E|^2$) profiles for the fundamental mode are superimposed on top of each structural schematic. d) Polar plots of far-field mode profiles. The left-hand (right-hand) semicircle corresponds to a ring-CBG (hole-CBG). e) Cross-sectional far-field mode profiles as a function of angle. f) Calculated collection efficiency in the upper half-sphere as a function of NA (P_{NA} / P_{upper}). g) Calculated Purcell factor (black line) and P_{NA} / P_{upper} with respect to wavelength for NAs of 0.7 (dashed blue line) and 0.12 (solid blue line), corresponding to the objective lens and the single-mode optical fiber, respectively.

A thin-membrane planar resonator with hole gratings produces an ultra-narrow vertical beam whose emission angle matches the small numerical aperture (NA) of a single-mode fiber. Using a pick-and-place technique,^[39] the fabricated hole-CBGs can be precisely integrated into the core of a single-mode fiber. The integrated fiber–QD system, as illustrated in **Figure 1a**, enables the compact plug-and-play operation of single photons from a source to a detector with high coupling efficiency and long-term stability.

2. Optimized Design of the Fiber-Interfacing Photonic Device

2D CBGs can provide a suitable thin membrane structure with a Gaussian far-field profile for fiber integration.^[40] However, the mismatch between the mode size of high-index nanophotonic cavities and low-index single-mode fibers still limits the fiber-coupling efficiency. Several design modifications, such as partially etched CBGs^[41] and hybrid CBGs,^[42–44] have been proposed to improve light extraction and coupling efficiency. Particularly, hybrid CBGs exhibit a high mode-coupling efficiency of more than 50% with a standard single-mode fiber (SMF28) in simulations; however, such fiber-coupled devices are yet to be reported in an experiment. To overcome the limitations and difficulties of the CBGs based on concentric ring arrays, we newly designed CBGs based on hole arrays. Hole-CBGs have distinct advantages over ring-based CBGs (ring-CBGs) in terms of several factors related to their hole systems. First, according to the effective medium theory,^[45,46] hole-CBGs can lower the refractive index contrast between air and matter (InP) than ring-CBGs. A

smooth refractive index gradient in hole-CBGs enlarges the spatial mode size. Moreover, hole-CBGs optimize the structural parameters in both the radial and axial directions, whereas ring-CBGs optimize the structure parameter only in the radial direction. This additional degree of freedom provided by hole-CBGs enables further optimization of constructive and destructive interferences, resulting in highly enhanced vertical emission and suppressed higher-order diffraction.^[47]

To study the fundamental capability of vertical beaming, we compared hole- and ring-CBGs on a thin membrane. Each structure was optimized using a finite-difference time-domain method at a target wavelength of 1250 nm to match the emission of InAs/InP QDs we studied.

In a ring-CBG, the wavelength of the fundamental cavity mode mostly depends on the radial period (Λ) of the concentric rings that satisfy the second-order Bragg condition, $\Lambda = \lambda_{QD} / n_{eff}$ (n_{eff} is an effective refractive index of a transverse electric mode).^[48] By iteratively changing the radius of the center disk (c) and the trench width between the rings (w), we optimized the structural parameters to achieve the maximum collection efficiency within a half-angle of 7° , which corresponds to the NA of a single-mode fiber. The optimized structural parameters of the ring-CBG were $\Lambda = 497$ nm, $c = 546$ nm, and $w = 149$ nm (Figure S1, Supporting Information). The thickness (T) of the structure was fixed at 280 nm to match that of the QD sample. To imitate QDs, we inserted two orthogonally polarized in-plane dipoles at the center of the structure. For the hole-CBGs, we similarly simulated the structure with the radial period between holes (Λ) and the radius of the center disk (c). The hole size (h) was considered for the

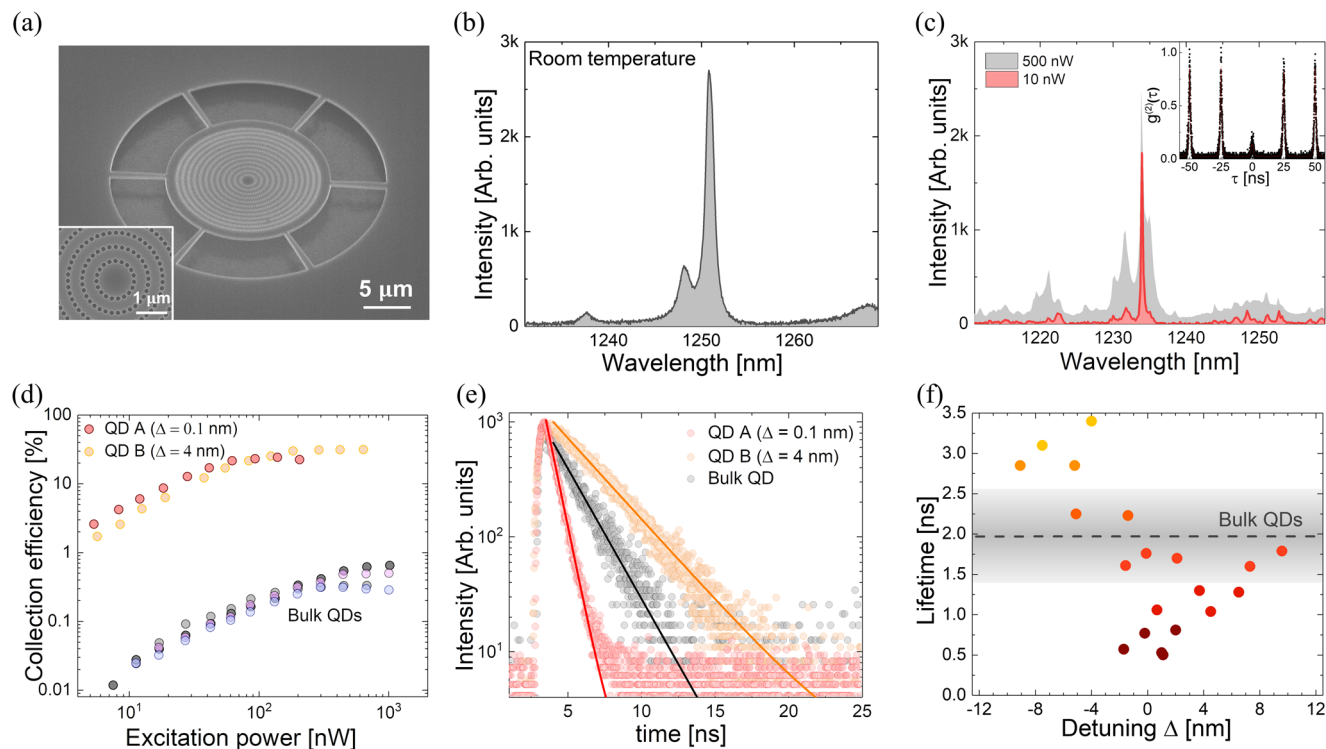


Figure 2. Optical characteristics of the hole-CBG device. a) SEM image of the fabricated hole-CBG. The inset shows a close-up view of the center of the device. b) Room temperature PL spectrum of the cavity mode of the fabricated hole-CBG. c) Low temperature (4 K) PL spectrum of the hole-CBG at 500 nW (gray curve) and 10 nW (red curve). The inset shows an antibunching curve for single QD emission. d) Collection efficiency of QD A (red circle) and QD B (orange circle) in the hole-CBG with spectral detuning values of 0.1 and 4 nm, respectively. Collection efficiencies of four different bulk QDs (gray, dark gray, blue, and purple) are plotted together for comparison. e) Decay curves of QDs A (red circle) and B (orange circle) in the hole-CBG along with that of a bulk QD (black circle). The solid lines are fitted single-exponential curves with decay times of 0.66 ns (red), 3.07 ns (orange), and 2 ns (black). f) Statistical distribution of the decay times of cavity-coupled QDs as a function of spectral detuning (Δ) between the cavity and the QDs. The dashed black line (gray-colored area) corresponds to the average value (standard deviation) of the lifetimes of the bulk QDs.

hole-CBG instead of the trench width (w) of the ring-CBG. Note that the hole-CBG structure has an additional parameter of the axial period between holes (a). The optimized structures had parameters of $\Lambda = 467$ nm, $c = 618$ nm, $h = 135$ nm, and $a = 210$ nm (Figure S1, Supporting Information).

Figure 1b,c shows the structural design with the superimposed in-plane cavity mode and the vertical cross-sectional emission profiles of the ring- and hole-CBGs at the fundamental cavity mode wavelength. The in-plane spatial mode of the hole-CBG is distributed over a wide area, which is in contrast with the tightly confined mode in the central disk of the ring-CBG. The larger mode size of the hole-CBG leads to more directional emission with a smaller divergence compared to the ring-CBG. This is clearly shown in the vertical cross-sectional field ($\log(|E|^2)$) profiles of the ring- and hole-CBGs in Figure 1b,c. Figure 1d compares the far-field patterns of the two structures plotted against angle and shows that the hole-CBG enables narrower Gaussian far-field emission. For the hole-CBG, most emissions lay within $\text{NA} = 0.12$ of the single-mode fiber. Meanwhile, a considerable collection loss is expected in the ring-CBG at small NAs. In Figure 1e, the cross-sectional far-field profiles with respect to angle show that the hole-CBG suppresses high-order diffraction. In contrast, the ring-CBG produces noticeable emissions into higher-order diffraction angles greater than 30° . To

quantify the vertical directionality of the two structures, we calculated the collection efficiency in the upper half-sphere, which is defined here as the ratio of the upward emission that passes through corresponding NAs to the total upper half-sphere emission ($P_{\text{NA}}/P_{\text{upper}}$). Figure 1f compares the simulated collection efficiencies of the ring- and hole-CBGs with respect to NA. As expected, the hole-CBG maintains high collection efficiencies, even at small NAs. In the case of the ring-CBG, only 24% of the emitted light can be collected with 0.12 NA, whereas the hole-CBG can collect as much as 63%. Figure 1g shows the simulated mode spectrum of an optimized hole-CBG at 1250 nm. The cavity mode of the hole-CBG exhibits a Q -factor of 4200 and a Purcell factor of over 100. This is considerably larger than the Q -factor (230) and Purcell factor (20) of the ring-CBG (Figure S1, Supporting Information). Although high Purcell enhancement occurs within a small spectral window of 0.38 nm at the resonant wavelength, high collection efficiency takes place over a broad spectral range, as shown in Figure 1g. This is advantageous for spectral coupling with solid-state quantum emitters.

3. Device Fabrication and Optical Characterization

To fabricate the designed hole-CBG, we used self-assembled InAs QDs with a density of $\approx 10 \mu\text{m}^{-2}$ located in the middle of

a 280 nm-thick InP membrane on a 2 μm -thick AllnAs sacrificial layer. The emissions of the QD ensemble span a broad spectral range from 1200 to 1550 nm, covering the telecom O- and C-bands. In this study, the short-wavelength region around 1250 nm, where the density of the QDs is relatively low, was designated as the center of the cavity mode to obtain single QD emissions with low background fluorescence. The hole-CBG device was fabricated on an InAs/InP QD wafer using electron-beam lithography followed by dry and wet etching processes. **Figure 2a** shows a scanning electron microscopy (SEM) image of the fabricated air-suspended hole-CBG.

We first characterized the mode spectrum of the hole-CBG at room temperature. **Figure 2b** shows photoluminescence (PL) from the cavity mode near the target wavelength of 1250 nm. With a lower Q -factor of 1020 than the simulated value (4200), the fabricated hole-CBG exhibits a double peak feature in the mode spectrum, which we attribute to the structural asymmetry of the fabricated device (**Figure S2**, Supporting Information).

To investigate the optical properties of coupled single QDs, we conducted low-temperature (4 K) micro-PL measurements of the hole-CBG using a 40 MHz pulsed 785 nm laser and a microscope objective lens (0.7 NA) in free space. **Figure 2c** shows the PL spectra at high (500 nW) and low (10 nW) excitation powers. At low excitation power, the sharp transitions correspond to the ground state emission of single QDs. At high excitation power, the cavity emission dominates over the saturated single QD emissions and is visible at around 1235 nm. The blueshift of the cavity mode at low temperatures compared to that at room temperature is due to the temperature-dependent refractive index. A significant increase in the intensity occurs in the QDs near the cavity mode. To prove that the bright single QD peak corresponds to single-photon emission, we performed a second-order correlation ($g^{(2)}(\tau)$) measurement using a Hanbury-Brown and Twiss setup. The antibunching signal in the $g^{(2)}(\tau)$ curve is shown in the inset of **Figure 2c**. We fitted the correlation curve to two-sided exponential functions convolved with a Gaussian function that accounts for a limited detector response time of 200 ps^[49] and obtained $g^{(2)}(0) = 0.16 \pm 0.02$. The nonzero $g^{(2)}(0)$ is mostly due to the spectrally superimposed broad cavity emission. To quantify the brightness of single photons from the hole-CBG device, we calculated the collection efficiency at the first lens (0.7 NA) by carefully calibrating the efficiency of the system ($(0.64 \pm 0.04)\%$), including the detector efficiency (20%) (**Figure S3**, Supporting Information). As the multiphoton probability of a single QD increases with the excitation power, we separately measured $g_{\text{sat}}^{(2)}(0) = 0.395$ at the saturation power (P_{sat}) and take the multiphoton correction term $\sqrt{1 - g_{\text{sat}}^{(2)}(0)} = 0.778$ into account in the collection efficiency.^[50] Considering the above factors, we calculated the collection efficiency of two different QDs (QD A and QD B) in the hole-CBG with different amounts of spectral detuning (0.1 and 4 nm, respectively) and compared the values with that of bulk QDs (**Figure S4**, Supporting Information). As shown in **Figure 2d**, the bulk QDs exhibit an expectedly low collection efficiency of less than 1%, whereas QD A and QD B in the hole-CBG exhibit a significantly higher collection efficiency of 24.3% and 30.1%, respectively. These results indicate that a large enhancement in the collection efficiency occurs over a wide spectral range, as expected based on the simulation in **Figure 2b**. We

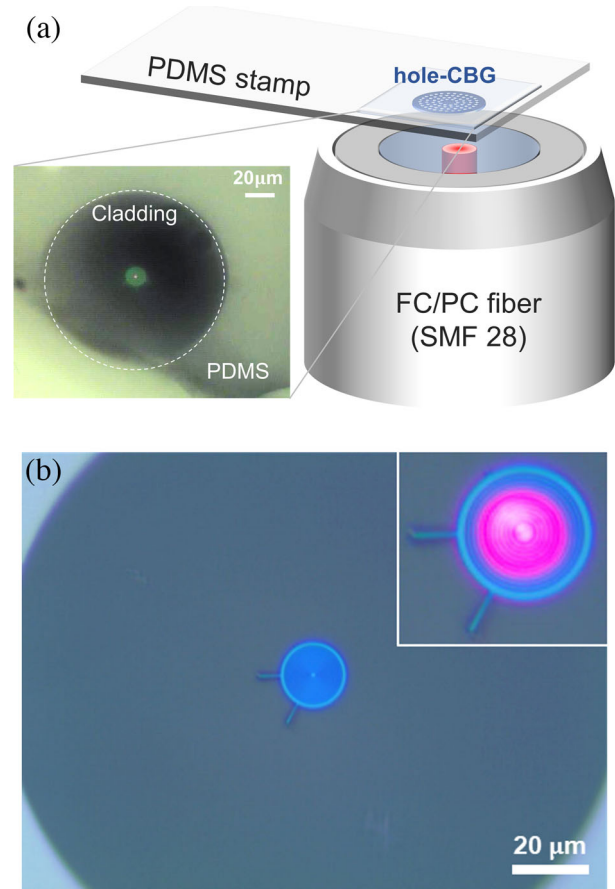


Figure 3. Integration of a single hole-CBG device into an FC/PC fiber. a) Schematic of the integration process between a single hole-CBG and a single-mode fiber (SMF28) using a PDMS stamp. The inset is an optical microscopy image ($\times 50$), which shows that the hole-CBG is aligned with the fiber core during the transfer process. b) Optical microscopy image of the hole-CBG transferred onto the end facet of the fiber. The inset shows a close-up image of the fiber core illuminated by a 633 nm laser beam sent from the opposite end of the fiber.

attribute the discrepancy between the simulated and measured collection efficiencies at 0.7 NA to the spatial mismatch between the QDs and the cavity mode and to the imperfections in the fabricated device (**Figure S5**, Supporting Information). In addition, it should be noted that the simulation only considered upward emission from the hole-CBG; therefore, a good bottom reflector will be required to achieve the simulated collection efficiency in the upper half-sphere.

As well as increasing the brightness, the Purcell effect in cavities affects the recombination dynamics of coupled QDs. **Figure 2e** shows the decay curves of cavity-coupled QDs A and B with different levels of detuning and compares them with that of a bulk QD. In the studied sample, bulk QDs have an average decay time of (1.97 ± 0.6) ns. Cavity resonant QD A has a rapid decay time of 0.66 ns, whereas QD B, with a large spectral detuning of 4 nm, shows a slow decay time of 3.07 ns. These results show that brightness enhancement occurs in a broad spectrum, but Purcell enhancement requires more restricted spectral matching with the cavity. **Figure 2f** shows a statistical distribution of the de-

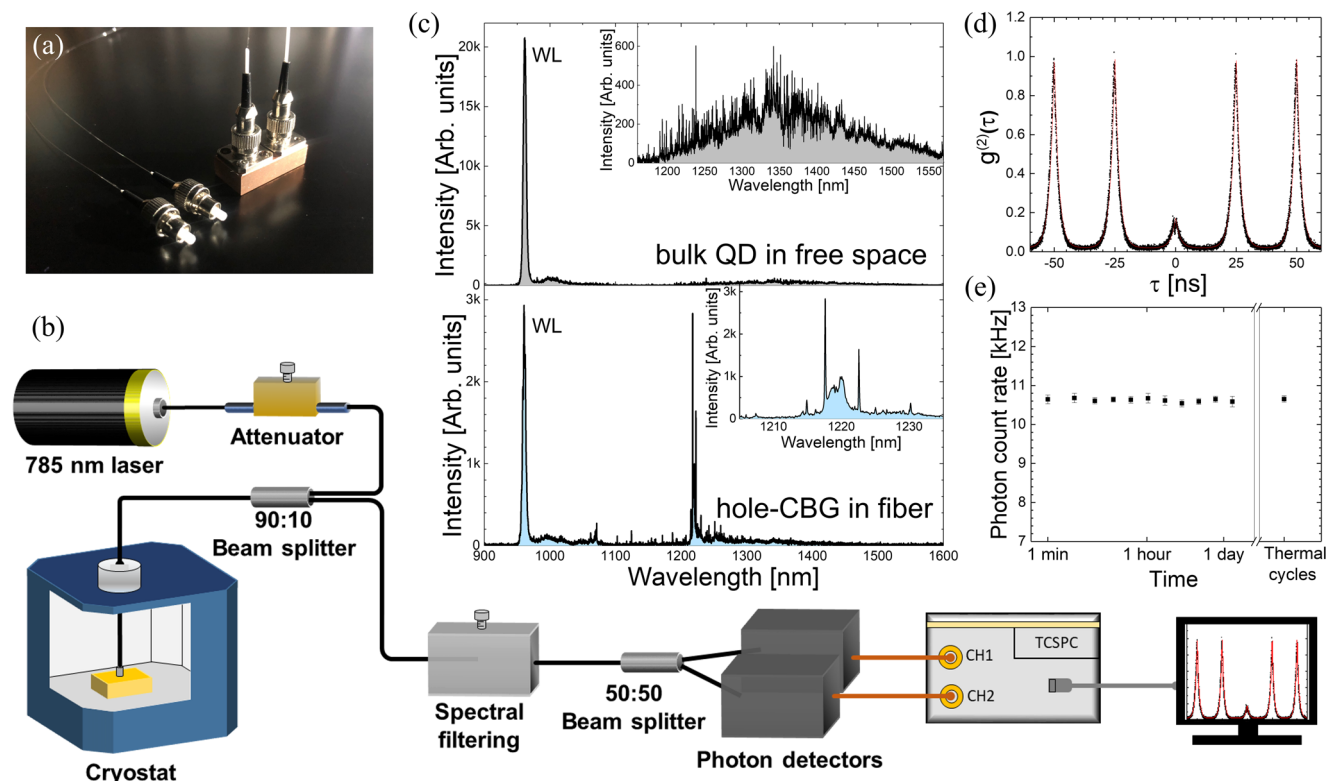


Figure 4. All-fiber coupled single-photon system. a) Photograph of the fiber–QD device installed on a cold finger. b) Schematic of the all-fiber coupled optical setup from the source to the detectors. c) Comparison of the PL spectra between the bulk QD sample measured in free space ($NA = 0.7$) (top) and the single hole-CBG device integrated with a single-mode fiber ($NA = 0.12$) (bottom). WL denotes wetting layer emission at ≈ 970 nm. The insets are close-up views of the QD emissions of each spectrum. d) Autocorrelation curve ($g^{(2)}(\tau)$) of single QD emission from the fiber–QD device. e) Intensity plot of the single-photon count rate of the fiber–QD device against time and thermal cycles.

decay times of QDs in different hole-CBGs as a function of spectral detuning. From the power- and polarization-dependent measurements, we predominantly observed the neutral exciton states of the QDs, including QD A and QD B in the hole-CBG. An enhancement in the decay rate up to four compared to the average lifetime of bulk QDs can be observed near the cavity mode.

4. Integration of a Single Hole-CBG Device into a Single-Mode Fiber

An important figure-of-merit for fiber-coupled quantum emitters is the coupling efficiency of single photons over a single-mode fiber. To demonstrate a fiber-integrated hole-CBG device, we employed a pick-and-place technique based on a polydimethylsiloxane (PDMS) stamp.^[51] As shown in Figure 2a, the fabricated hole-CBG device is air-suspended by thin tethers in the QD wafer. The transparent PDMS stamp on a glass slide can easily detach a single hole-CBG from the QD wafer and transfer it to the core of the fiber. The process was monitored in real-time using an optical microscope, as shown in Figure 3a. To align the central axis of the device with the core of the fiber, a red (633 nm) laser beam was sent from the opposite end of the fiber. Figure 3b shows an optical image of the end facet of the single-mode fiber after integration of the single hole-CBG device. The hole-CBG device is firmly attached to the fiber via van der Waals forces and well-centered at the fiber core with high accuracy (<500 nm) (Figure S6, Sup-

porting Information). The integrated fiber–QD device was then mounted on an Au-coated cold finger that serves as a back reflector and thermal conductor for low-temperature measurements. For the fiber-coupled hole-CBGs, we separately simulated a fiber-coupling efficiency as the ratio of the power flux through the fundamental mode of the single-mode fiber to the total dipole power and estimated the fiber-coupling efficiency of 53%, including the bottom reflection (Figure S7, Supporting Information). In addition, the integration of hole-CBGs into the fiber shifts the mode wavelength and lowers Purcell and Q factors (Figure S7, Supporting Information).

5. Bright and Stable Single Photons in an All-Fiber Coupled System

Figure 4a shows a photographic image of the fiber–QD device mounted on a cold finger for low-temperature measurements. The use of an FC/PC-connectorized fiber enabled the fiber–QD device to be mounted on a cold finger using conventional FC/PC mating sleeves. After mounting the integrated fiber–QD device on the cryostat, the fiber inside the cryostat was connected to the fiber outside via a fiber feedthrough installed in the cryostat lid. We sent a 785 nm pumping laser and collected the QD emission through the fiber using a 90:10 fiber beam splitter. To measure single photons, we spectrally filtered out a single QD emission using a fiber-based tunable filter (resolution = 0.01 nm) and sent

single photons to a fiber-based 50:50 beam splitter followed by fiber-coupled InGaAs single-photon detectors. A schematic of an all-fiber coupled system from the single-photon source to the detector is shown in Figure 4b. Figure 4c compares the PL spectrum of bulk QDs measured in free space (top) with that of the hole-CBG directly coupled to a single-mode fiber (bottom). The strong emissions close to 970 nm correspond to a wetting layer. In free space, the bulk QDs exhibit very weak emissions from 1200 to 1550 nm, even with a high NA = 0.7 objective lens. For the fiber-QD device, the PL spectrum clearly reveals that the hole-CBG device efficiently out-couples the spectrally coupled QD emissions into the single-mode fiber (0.12 NA).

Figure 4d shows a $g^{(2)}(\tau)$ curve of the spectrally filtered single QD emission from the fiber-QD device. The observed $g^{(2)}(0)$ is 0.16 ± 0.02 from fitting with no background subtraction. To estimate the brightness, we excited the QD at a low repetition rate of 2.5 MHz, which prevented saturation effects in the InGaAs single-photon detector, and counted a single-photon detection rate of (10.63 ± 0.11) kHz at P_{sat} . To calculate the QD to fiber-coupling efficiency, we separately measured the system efficiency ($(4.6 \pm 0.3)\%$), including the detector efficiency (20%), and then calibrated the multiphoton events, where $g_{\text{sat}}^{(2)}(0) = 0.24$ at P_{sat} (Figure S3, Supporting Information). This results in a QD-to-fiber coupling efficiency of $(8.1 \pm 0.5)\%$. If we consider typical 80 MHz pulsed excitation, this value corresponds to a single-photon rate of 6.5 MHz at the end of the first fiber. Although the achieved fiber-coupling efficiency of 8.1% is lower than the simulated coupling efficiency of 53%, the measured single-photon coupling efficiency is a record high for fiber-integrated QD devices at telecom wavelengths.^[35,52,53] The nonideal position of the QD in the hole-CBG device, the spatial misalignment between the hole-CBG device and fiber core, and imperfect fabrications may explain the lower experimental coupling efficiency (Figures S5 and S6, Supporting Information). In addition, InAs/InP QDs might have non-unit internal efficiency, even at low temperatures.^[54] Therefore, the measured value provides a lower bound for the possible coupling efficiency.

Finally, we investigated the long-term stability of the fiber-QD device. The single-photon count rates at P_{sat} of the device are plotted against time in Figure 4e. We observed intensity fluctuations within 1%, mostly originating from fluctuations in the laser power. These stable count rates were maintained even after multiple thermal cycles. As any optical alignment is not necessary in an all-fiber coupled single-photon system, this system ensures long-term stability.

6. Conclusions

In this study, we have successfully demonstrated the efficient and reliable transmission of single photons from single QDs into an all-fiber coupled system. A hole-based diffraction cavity generates a narrow Gaussian emission that matches the small NA of a standard single-mode fiber at telecom wavelengths. The thin membrane structure combined with a pick-and-place technique enables the simple and robust integration of a single QD device into an FC/PC-connectorized fiber.

Regarding the design of hole-CBGs, we studied simple hole arrays with fixed sizes and periodicity on a thin membrane. The

configuration of the hole arrays could be optimized further by adding more variations in hole size and positions. Machine learning techniques can be used to optimize such variations.^[55] Introducing site-selective growth of QDs^[56] and deterministic cavity integration methods^[57] can increase the coupling efficiency up to the theoretical limit.

With the rapid development of quantum photonic technologies, the demand for practical quantum light sources is increasing in various fields, including quantum imaging, quantum diagnostics, and quantum simulation using photons. Our approach could provide practical and reliable plug-and-play quantum light devices for all-fiber connectorized quantum information processing from sources to detectors. Moreover, integrated quantum emitters with spin states could enable the implementation of quantum memories and repeaters in fiber networks. Therefore, our approach can be extended to distribute quantum states and connect quantum nodes on commercialized fiber channels.

Supporting Information

Supporting Information is available from the Wiley Online Library or from the author.

Acknowledgements

The authors would like to acknowledge support from the National Research Foundation of Korea grant funded by the Korea government (MSIT) (NRF-2020M3H3A1098869, NRF-2022R1A2C2003176) and Institute of Information and Communications Technology Planning and Evaluation (IITP) grant funded by the Korea government (MSIT) (No. 2019-0-00434), the ITRC (Information Technology National Research Center) support program (IITP 2022-2020-0-01606) supervised by the IITP, the UBSI Research Fund (1.210116.01) of Ulsan National Institute of Science & Technology (UNIST), and the Air Force Office of Scientific Research (Grant No. FA23862014072).

Conflict of Interest

The authors declare no conflict of interest.

Data Availability Statement

The data that support the findings of this study are available from the corresponding author upon reasonable request.

Keywords

fiber integration, quantum dots, quantum photonics, single-photon source

Received: February 25, 2022

Revised: July 1, 2022

Published online:

[1] P. Senellart, G. Solomon, A. White, *Nat. Nanotechnol.* **2017**, *12*, 1026.

[2] I. Aharonovich, D. Englund, M. Toth, *Nat. Photonics* **2016**, *10*, 631.

[3] H. Wang, J. Qin, X. Ding, M.-C. Chen, S. Chen, X. You, Y.-M. He, X. Jiang, L. You, Z. Wang, *Phys. Rev. Lett.* **2019**, *123*, 250503.

- [4] S. F. C. da Silva, G. Undeutsch, B. Lehner, S. Manna, T. M. Krieger, M. Reindl, C. Schimpf, R. Trotta, A. Rastelli, *Appl. Phys. Lett.* **2021**, *119*, 120502.
- [5] C. Schimpf, M. Reindl, D. Huber, B. Lehner, F. Covre Da Silva Saimon, S. Manna, M. Vyvlecka, P. Walther, A. Rastelli, *Sci. Adv.* **2021**, *7*, eabe8905.
- [6] F. Basso Basset, M. Valeri, E. Rocca, V. Muredda, D. Poderini, J. Neuwirth, N. Spagnolo, B. R. Michele, G. Carvacho, F. Sciarrino, R. Trotta, *Sci. Adv.* **2021**, *7*, eabe6379.
- [7] D. Press, K. De Greve, P. L. McMahon, T. D. Ladd, B. Friess, C. Schneider, M. Kamp, S. Höfling, A. Forchel, Y. Yamamoto, *Nat. Photonics* **2010**, *4*, 367.
- [8] H.-K. Lo, M. Curty, K. Tamaki, *Nat. Photonics* **2014**, *8*, 595.
- [9] N. Gisin, G. Ribordy, W. Tittel, H. Zbinden, *Rev. Mod. Phys.* **2002**, *74*, 145.
- [10] T. Gao, L. Rickert, F. Urban, J. Große, N. Srocka, S. Rodt, A. Musiał, K. Żołnaczyk, P. Mergo, K. Dybka, W. Urbańczyk, G. Sęk, S. Burger, S. Reitzenstein, T. Heindel, *Appl. Phys. Rev.* **2022**, *9*, 011412.
- [11] D. A. Vajner, L. Rickert, T. Gao, K. Kaymazlar, T. Heindel, *Adv. Quantum Technol.* **2022**, 2100116.
- [12] M. Reindl, D. Huber, C. Schimpf, F. C. da Silva Saimon, B. R. Michele, H. Huang, V. Zwiller, D. J. Klaus, A. Rastelli, R. Trotta, *Sci. Adv.* **2018**, *4*, eaau1255.
- [13] W. B. Gao, P. Fallahi, E. Togan, A. Delteil, Y. S. Chin, J. Miguel-Sanchez, A. Imamoğlu, *Nat. Commun.* **2013**, *4*, 2744.
- [14] S. Sun, H. Kim, G. S. Solomon, E. Waks, *Nat. Nanotechnol.* **2016**, *11*, 539.
- [15] S. T. Yilmaz, P. Fallahi, A. Imamoğlu, *Phys. Rev. Lett.* **2010**, *105*, 033601.
- [16] S. Sun, H. Kim, Z. Luo, S. S. Glenn, E. Waks, *Science* **2018**, *361*, 57.
- [17] R. Uppu, L. Midolo, X. Zhou, J. Carolan, P. Lodahl, *Nat. Nanotechnol.* **2021**, *16*, 1308.
- [18] I. Schwartz, D. Cogan, E. R. Schmidgall, Y. Don, L. Gantz, O. Kenneth, N. H. Lindner, D. Gershoni, *Science* **2016**, *354*, 434.
- [19] S. Meesala, Y.-I. Sohn, B. Pingault, L. Shao, H. A. Atikian, J. Holzgrafe, M. Gündoğan, C. Stavrakas, A. Sipahigil, C. Chia, *Phys. Rev. B* **2018**, *97*, 205444.
- [20] T. Hummel, C. Ouellet-Plamondon, E. Ugur, I. Kulkova, T. Lund-Hansen, M. A. Broome, R. Uppu, P. Lodahl, *Appl. Phys. Lett.* **2019**, *115*, 021102.
- [21] J.-H. Kim, C. J. K. Richardson, R. P. Leavitt, E. Waks, *Nano Lett.* **2016**, *16*, 7061.
- [22] H. Kim, J. S. Moon, G. Noh, J. Lee, J.-H. Kim, *Nano Lett.* **2019**, *19*, 7534.
- [23] B. Alén, F. Bickel, K. Karrai, R. J. Warburton, P. M. Petroff, *Appl. Phys. Lett.* **2003**, *83*, 2235.
- [24] X. You, M.-Y. Zheng, S. Chen, R.-Z. Liu, J. Qin, M.-C. Xu, Z.-X. Ge, T.-H. Chung, Y.-K. Qiao, Y.-F. Jiang, H.-S. Zhong, M.-C. Chen, H. Wang, Y.-M. He, X.-P. Xie, H. Li, L.-X. You, C. Schneider, J. Yin, T.-Y. Chen, M. Benyoucef, Y.-H. Huo, S. Hoefling, Q. Zhang, C.-Y. Lu, J.-W. Pan, (*Preprint*) *arXiv*. 2106.15545, v1, unpublished.
- [25] K. Takemoto, Y. Nambu, T. Miyazawa, Y. Sakuma, T. Yamamoto, S. Yorozu, Y. Arakawa, *Sci. Rep.* **2015**, *5*, 14383.
- [26] X. Xu, I. Toft, R. T. Phillips, J. Mar, K. Hammura, D. A. Williams, *Appl. Phys. Lett.* **2007**, *90*, 061103.
- [27] G. Muñoz-Matutano, D. Barrera, C. R. Fernández-Pousa, R. Chulia-Jordan, L. Seravalli, G. Trevisi, P. Frigeri, S. Sales, J. Martínez-Pastor, *Sci. Rep.* **2016**, *6*, 27214.
- [28] H. Kumano, T. Harada, I. Suemune, H. Nakajima, T. Kuroda, T. Mano, K. Sakoda, S. Odashima, H. Sasakura, *Appl. Phys. Express* **2016**, *9*, 032801.
- [29] A. Muller, E. B. Flagg, M. Metcalfe, J. Lawall, G. S. Solomon, *Appl. Phys. Lett.* **2009**, *95*, 173101.
- [30] O. Ortiz, F. Pastier, A. Rodriguez, Priya, A. Lemaitre, C. Gomez-Carbonell, I. Sagnes, A. Harouri, P. Senellart, V. Giesz, M. Esmann, N. D. Lanzillotti-Kimura, *Appl. Phys. Lett.* **2020**, *117*, 183102.
- [31] H. Snijders, J. A. Frey, J. Norman, V. P. Post, A. C. Gossard, J. E. Bowers, M. P. van Exter, W. Löffler, D. Bouwmeester, *Phys. Rev. Appl.* **2018**, *9*, 031002.
- [32] D. B. Northeast, D. Dalacu, J. F. Weber, J. Phoenix, J. Lapointe, G. C. Aers, P. J. Poole, R. L. Williams, *Sci. Rep.* **2021**, *11*, 22878.
- [33] A. Schlehahn, S. Fischbach, R. Schmidt, A. Kaganskiy, A. Strittmatter, S. Rodt, T. Heindel, S. Reitzenstein, *Sci. Rep.* **2018**, *8*, 1340.
- [34] P.-I. Schneider, N. Srocka, S. Rodt, L. Zschiedrich, S. Reitzenstein, S. Burger, *Opt. Express* **2018**, *26*, 8479.
- [35] A. Musiał, K. Żołnaczyk, N. Srocka, O. Kravets, J. Große, J. Olszewski, K. Poturaj, G. Wójcik, P. Mergo, K. Dybka, M. Dyrkacz, M. Dłubek, K. Lauritsen, A. Bültner, P.-I. Schneider, L. Zschiedrich, S. Burger, S. Rodt, W. Urbańczyk, G. Sęk, S. Reitzenstein, *Adv. Quantum Technol.* **2020**, *3*, 2000018.
- [36] C.-M. Lee, M. A. Buyukkaya, S. Aghaeimeibodi, A. Karasahin, C. J. K. Richardson, E. Waks, *Appl. Phys. Lett.* **2019**, *114*, 171101.
- [37] D. Cadeddu, J. Teissier, F. R. Braakman, N. Gregersen, P. Stepanov, J.-M. Gérard, J. Claudon, R. J. Warburton, M. Poggio, M. Munsch, *Appl. Phys. Lett.* **2016**, *108*, 011112.
- [38] T. G. Tietze, K. P. Nayak, J. D. Thompson, T. Peyronel, N. P. de Leon, V. Vuletić, M. D. Lukin, *Optica* **2015**, *2*, 70.
- [39] J.-H. Kim, S. Aghaeimeibodi, J. Carolan, D. Englund, E. Waks, *Optica* **2020**, *7*, 291.
- [40] L. Li, E. H. Chen, J. Zheng, S. L. Mouradian, F. Dolde, T. Schröder, S. Karaveli, M. L. Markham, D. J. Twitchen, D. Englund, *Nano Lett.* **2015**, *15*, 1493.
- [41] M. Davanço, M. T. Rakher, D. Schuh, A. Badolato, K. Srinivasan, *Appl. Phys. Lett.* **2011**, *99*, 041102.
- [42] B. Yao, R. Su, Y. Wei, Z. Liu, T. Zhao, J. Liu, *JKPS* **2018**, *73*, 1502.
- [43] A. Barbiero, J. Huwer, J. Skiba-Szymanska, T. Müller, R. M. Stevenson, A. J. Shields, *Opt. Express* **2022**, *30*, 10919.
- [44] L. Rickert, T. Kupko, S. Rodt, S. Reitzenstein, T. Heindel, *Opt. Express* **2019**, *27*, 36824.
- [45] S. Tang, B. Zhu, M. Jia, Q. He, S. Sun, Y. Mei, L. Zhou, *Phys. Rev. B* **2015**, *91*, 174201.
- [46] W. Gao, W. S. L. Lee, C. Fumeaux, W. Withayachumnankul, *APL Photonics* **2021**, *6*, 076105.
- [47] L. Kipp, M. Skibowski, R. L. Johnson, R. Berndt, R. Adelung, S. Harm, R. Seemann, *Nature* **2001**, *414*, 184.
- [48] S. Ates, L. Sapienza, M. Davanco, A. Badolato, K. Srinivasan, *IEEE J. Sel. Top. Quantum Electron.* **2012**, *18*, 1711.
- [49] J.-H. Kim, T. Cai, C. J. K. Richardson, R. P. Leavitt, E. Waks, *Optica* **2016**, *3*, 577.
- [50] O. Gazzano, S. M. De Vasconcellos, C. Arnold, A. Nowak, E. Galopin, I. Sagnes, L. Lanco, A. Lemaître, P. Senellart, *Nat. Commun.* **2013**, *4*, 1425.
- [51] M. E. Reimer, G. Bulgarini, N. Akopian, M. Hocevar, M. B. Bavinck, M. A. Verheijen, E. P. A. M. Bakkers, L. P. Kouwenhoven, V. Zwiller, *Nat. Commun.* **2012**, *3*, 737.
- [52] C.-M. Lee, M. A. Buyukkaya, S. Aghaeimeibodi, A. Karasahin, C. J. K. Richardson, E. Waks, *Appl. Phys. Lett.* **2019**, *114*, 171101.
- [53] X. Xu, F. Brossard, K. Hammura, D. A. Williams, B. Alloing, L. H. Li, A. Fiore, *Appl. Phys. Lett.* **2008**, *93*, 021124.
- [54] C. J. Richardson, R. P. Leavitt, J.-H. Kim, E. Waks, I. Arslan, B. Arey, *J. Vac. Sci. Technol., B* **2019**, *37*, 011202.
- [55] T. Asano, S. Noda, *Opt. Express* **2018**, *26*, 32704.
- [56] I. S. Han, Y.-R. Wang, M. Hopkinson, *Appl. Phys. Lett.* **2021**, *118*, 142101.
- [57] L. Sapienza, M. Davanço, A. Badolato, K. Srinivasan, *Nat. Commun.* **2015**, *6*, 7833.